

Analysis of differential scanning calorimetry (DSC)

determining the transition temperatures, and enthalpy and heat capacity changes in multicomponent systems by analytical model fitting

Ghanbari, Elmira; Picken, Stephen J.; van Esch, Jan H.

DOI

[10.1007/s10973-023-12356-1](https://doi.org/10.1007/s10973-023-12356-1)

Publication date

2023

Document Version

Final published version

Published in

Journal of Thermal Analysis and Calorimetry

Citation (APA)

Ghanbari, E., Picken, S. J., & van Esch, J. H. (2023). Analysis of differential scanning calorimetry (DSC): determining the transition temperatures, and enthalpy and heat capacity changes in multicomponent systems by analytical model fitting. *Journal of Thermal Analysis and Calorimetry*, 148(22), 12393-12409. <https://doi.org/10.1007/s10973-023-12356-1>

Important note

To cite this publication, please use the final published version (if applicable). Please check the document version above.

Copyright

Other than for strictly personal use, it is not permitted to download, forward or distribute the text or part of it, without the consent of the author(s) and/or copyright holder(s), unless the work is under an open content license such as Creative Commons.

Takedown policy

Please contact us and provide details if you believe this document breaches copyrights. We will remove access to the work immediately and investigate your claim.



Analysis of differential scanning calorimetry (DSC): determining the transition temperatures, and enthalpy and heat capacity changes in multicomponent systems by analytical model fitting

Elmira Ghanbari¹ · Stephen J. Picken¹ · Jan H. van Esch¹

Received: 5 January 2023 / Accepted: 2 July 2023
© The Author(s) 2023

Abstract

We have developed an analytical method to quantitatively analyze differential scanning calorimetry (DSC) experimental data. This method provides accurate determination of thermal properties such as equilibrium melting temperature, latent heat, change of heat capacity which can be performed automatically without intervention of a DSC operator. DSC is one of the best techniques to determine the thermal properties of materials. However, the accuracy of the transition temperature and enthalpy change can be affected by artifacts caused by the instrumentation, sampling, and the DSC analysis methods which are based on graphical constructions. In the present study, an analytical function ($DSC_N(T)$) has been developed based on an assumed Arrhenius crystal size distribution together with instrumental and sample-related peak broadening. The $DSC_N(T)$ function was successfully applied to fit the experimental data of a substantial number of calibration and new unknown samples, including samples with an obvious asymmetry of the melting peak, yielding the thermal characteristics such as melting and glass transition temperature, and enthalpy and heat capacity change. It also allows very accurate analysis of binary systems with two distinct but severely overlapping peaks and samples that include a cold crystallization before melting.

Keywords DSC · Analytical function · Melting temperature · Glass transition · Crystallization · Change in heat capacity and enthalpy

Introduction

Differential scanning calorimetry (DSC) is a widely and commonly used thermoanalytical technique to characterize the thermal properties of materials such as transition temperature (T°) and change in enthalpy (ΔH) [1]. There are different types of DSC technique such as heat flux and power compensation. In power compensation DSC, the heat flow in the form of electrical power is measured by the instrument as a function of time (isothermal experiments) or temperature (non-isothermal experiments), respectively. The principle underlying the power compensating DSC is that during endothermic or exothermic chemical reactions or physical phase transitions occurring in the sample, a compensating power needs to be released or absorbed in a sample relative

to the reference. In fact, the furnace is heated up or down at a constant rate to keep the temperature of the sample and reference the same. The difference in the heat flow is due to the difference in the heat capacity of the sample and the reference which appears as an endothermic or exothermic peak in the DSC trace [2].

The DSC trace recorded for melting of an ideal sample, fully crystalline or 100% pure compound with a low thermal resistance, is in theory an infinitely sharp precisely defined temperature, which could be imagined as a delta function spike in the heat capacity (Fig. 1a) [3]. However, in practice DSC records the heat flow as a distribution, which for simplicity could be assumed to be a Gaussian bell-shaped curve (Fig. 1a). The Gaussian broadening is a combination of some artifacts caused by sampling (such as mass and geometry), the sample quality itself (such as the presence of a distribution of crystal sizes and/or impurities), and the instrumentation which may cause the sharp symmetric DSC peak turning into an asymmetric distribution as schematically shown in Fig. 1b. The instrumental artifacts may be due to imbalances in the instrument which can cause instrument

✉ Jan H. van Esch
j.h.vanesch@tudelft.nl

¹ Delft University of Technology, 2629 HZ Delft, The Netherlands

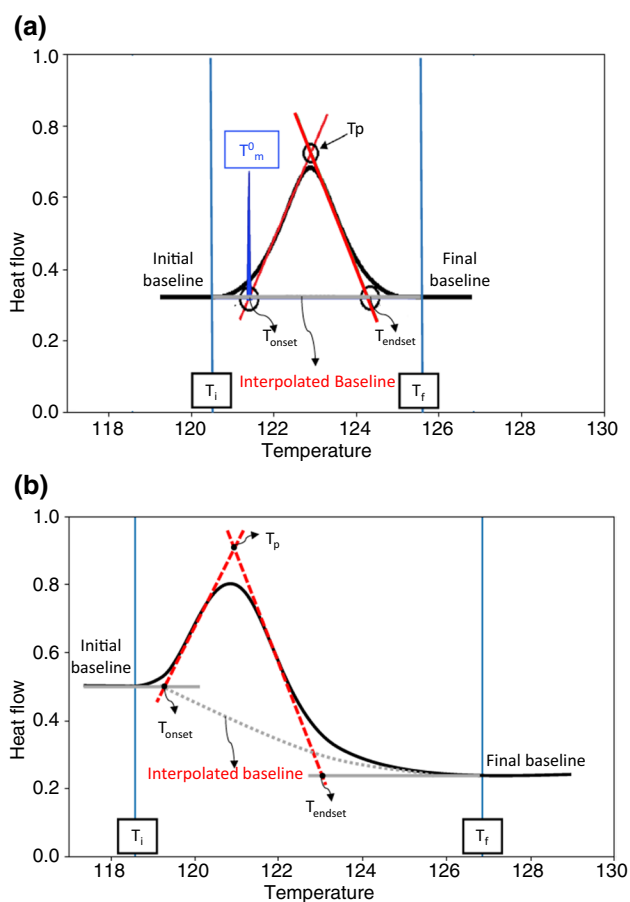


Fig. 1 Schematic anatomy of a DSC trace, the measured heat flow versus temperature: **(a)** sharp spike versus Gaussian distribution in the DSC trace with a flat baseline, T_{onset} is the temperature used as the calibration temperature, T_{cal} , **(b)** asymmetric endothermic peak with a skewed baseline

baseline features that include (at least) an offset, a slope, and a curvature. It can also be due to the heat capacity effects caused by the different thermal resistances of different compartments, in other words, the thermal conductivity through the outer and inner interfaces (calorimeter/pan and pan/sample respectively) which can reduce the resolution of the recorded trace [4].

Recorded DSC traces are usually analyzed by an operator via the built-in software of the DSC equipment. The determination of the key elements, such as the peak positions and peak area, is usually done manually for the further analysis which is typically as follows: the section of the curve between T_i , where the curve of measured values begins to deviate from the extrapolated initial baseline, and T_f , where it reaches again the extrapolated final baseline, is defined as the peak (Fig. 1). In practice, various methods are applied to interpolate the baseline between the initial and the final peak temperature. The linear extrapolations of the initial and final baseline are usually used to determine the extrapolated

onset and endset temperature of the peak. The point where the auxiliary line through the rising edge of the peak intersects the linearly extrapolated baseline is usually considered as the onset of transition, which is taken as the transition temperature during calibration; taking melting transition as an example, the temperature during the melting remains constant which is plausibly valid for reasonably uniform large crystalline materials with a high thermal conductivity such as metals [5]. The determination of the peak area with visual-manual examination is substantially subjective depending on the range of temperature selected by a data analyst for the integration of the area under the peak.

The possible errors due to the artifacts on top of the visual-manual examination of the DSC data necessitates a reliable method which can determine the main feature of the DSC trace by eliminating the possible variabilities, especially in the case of asymmetric and broad peaks. In this study, an analytical model, $\text{DSC}_N(T)$ function, has been developed to provide accurate and reproducible analysis of experimental DSC output data. The analytical model is based on thermodynamics concepts which takes the baseline features, limited instrumental resolution, and the sample-related effects into account to capture the key features of experimental DSC traces. It is based on the assumption that the sample crystalline structure develops via a rate-limited growth, for instance governed by the temperature-dependent viscosity which has been described by a simple Arrhenius activated process. This gives rise to a crystal size distribution which causes a distribution of melting points. Upon heating, the DSC trace will reflect this Arrhenius-like distribution of melting points. The model also includes the accuracy of the measurement which we assume is limited by a Gaussian smearing of the data which accounts for the shape of the peak.

Materials and method

Differential scanning calorimetry (DSC) measurement

All the DSC measurements in this study were performed on PerkinElmer-Pyris diamond Differential scanning calorimeter with two 1 g furnaces (working on the power-compensation temperature null principle with accuracy/precision: $< \pm 1\%$ / $< \pm 0.1\%$). Nitrogen (99.99% purity) was used to purge the thermal analysis system at a rate of 50 mL min^{-1} . Temperature and heat flow calibration were done by the heating scan of indium, a highly pure metal provided by PerkinElmer with accurately known enthalpies of fusion and melting point, $\Delta H_{\text{fusion}} = 6.80 \text{ cal g}^{-1}$ or 28.47 J g^{-1} and $T_m^0 = 156.4 \text{ }^\circ\text{C}$, under the same condition as the to-be-measured samples before each measurement. The onset of melting transition (T_{onset} in Fig. 1a) and the

area under the peak from T_i to T_f were chosen, respectively, for the calibration of the melting temperature and enthalpy of fusion.

Samples were weighed in an aluminum sample pan on a microbalance and the sample pan and an identical empty pan as the reference. Both sample and reference pans were covered by identical aluminum lid and placed in the furnaces of the DSC apparatus. Heating and cooling scans were run at the given heating rate, annotated by R , ($R = dT/dt$). Both pans were heated over a certain temperature range where the transition temperature of the compound is expected (at least 30 °C below and above the temperature range of interest). A first isothermal/heating scan was run followed by a fixed cooling cycle preceding a second heating cycle. The traces recorded for the second heating cycle were used for further analysis since their previous thermal history of the compounds through the synthesis or sample preparation has been eliminated via the first two cycles. Moreover, the pre-heating and cooling scans could also eliminate the sample geometry effect and provide the measurement with a sample with more flat and uniform layer with a proper contact with the bottom of the pan. The contact between the sample and the sample pan and the location of the pan in the crucible can affect the reproducibility of the extrapolated onset temperature of the melting peak. As the heat transfer between the sample and sample pan can change due to the fusion and this might influence the extrapolated peak onset temperature, each sample must be subjected to at least two subsequent measurements under the same condition.

To validate the applicability of $DSC_N(T)$ model for different materials, DSC experiments on a variety of organic and inorganic compounds were conducted and $DSC_N(T)$ model was fitted on the experimental data sets; two sets of experiments were performed on indium: (1) variable heating rates, investigated between 2 and 50 K min⁻¹ for a small sample of 7 mg and variable sample mass with constant heating rate of 2 K min⁻¹, for different samples within 1–54 mg. To assess the level of errors associated with the experiment and the fitting procedure, three samples with nearly identical mass from the identical benzoic acid (99%, Metler Toledo) were heated at 2 K min⁻¹. The heating of stearic acid with two different degrees of purity (95% and 97%, Sigma-Aldrich), poly((R)-3-hydroxybutyrate-co-(R)-3-hydroxyvalerate-co-(R)-3-hydroxyhexanoate), commonly known as PHBVH, with the composition of 3-hydroxyhexanoic acid content, 4.1%, 3-hydroxyvaleric acid content, 2.3%, PHH content, 4.1%, PHV content, 2.3% in powder form ($M_n = 1,000,000$, Sigma-Aldrich), and 8OCB (4'-octyloxy-4-cyanobiphenyl), commercially available in the form of powder (crystalline phase) were performed under the above-mentioned conditions. Likewise, the bisamide gelators varying in the number of bridging carbons between amide groups (5, 6, 7, 8, 9, and 10) used in all the experimental studies were synthesized

based on the protocol of our previous study [6]. Binary bisamides of 5BA6BA have been prepared by mixing the single 5BA and 6BA at different molar ratios which were mechanically stirred in the molten state. The subscripts show the molar ratio of the individual compounds; for example, (5BA)₁(6BA)₇ indicates that 5BA and 6BA were molecularly mixed in 1:7 molar ratio.

The initial estimation of the transition temperatures on the raw data of the DSC experiments was done by means of the built-in software of Diamond DSC machine, Pyris. Prior to the data collection for the analysis by Pyris or $DSC_N(T)$ analytical model, the heat flow of the raw data (mW) was normalized per mass of the sample (mg) resulting in 'normalized heat flows' (Wg⁻¹). The normalized data were transferred from the PerkinElmer computer into ASCII format. The data visualization has been done by Python, and in all graphs the endothermic peaks were plotted in upward direction. The nonlinear curve fitting has been done by Python programming language. Nonlinear least squares (NLLS) from `scipy.optimize.curve_fit` module have been used to fit the $DSC_N(T)$ function to the experimental data. It takes the independent variable and the function parameters and optimizes the parameters within a defined Lower and upper bounds to minimize the sum of squares of nonlinear functions. In some cases, a manual fitting was applied to improve the optimized parameters by finding the global minimum using the solver in Microsoft excel. The curve fitting consisted of the entire temperature range on the X-axis which is broad enough to cover the peak region and the precise baseline determination on the tails at both sides of the peak minimum. This improves the reproducibility of the fitting process and the precision of the fit statistics. For the purpose of improving the illustration resolution, the temperature ranges were further narrowed to the peak and baseline domain in all subsequent figures, although experimental data and fit are available over the entire experimental domain.

Theoretical principles and calculation of the analytical model ($DSC_N(T)$)

There are abundant models and theoretical methods explaining the thermodynamic of phase transitions in materials using DSC experimental data [7–16]. However, the quantitative description of DSC which can deconvolute the superposition of the underlying thermal phenomena is missed. In DSC trace of heat flow versus temperature, the slope is representative of the heat capacity of the samples (Eq. 1) (if the trace has been normalized with respect to the entire mass of the sample, then the slope is representative of the specific heat capacity) [17]. The heat capacity itself at T_m^0 in an ideal DSC measurement (Fig. 1a) would be infinite but in practice is a rather broad trace due to instrumental broadening, non-isothermal conditions, and impurity effect [1, 18, 19].

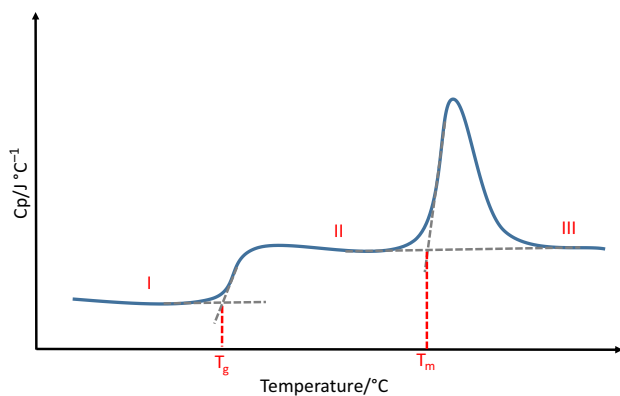


Fig. 2 A schematic DSC (C_p versus Temperature) of semi-crystalline polymers over the range of temperature where glass transition and melting transition occur at T_g and T_m , respectively

$$C_p = \frac{dH}{dT} \quad (1)$$

In fact, the DSC instrument measures the differential heat flow absorbed or released by the sample with respect to the reference in terms of the power which is the heat exchange rate (Eq. 2).

$$P(t) = \frac{dH}{dt} \quad (2)$$

By division of the fraction in Eq. 2 with respect to Eq. 1, Eq. 3 is obtained where R is the heating rate imposed by the instrument.

$$P(t) = \frac{dH}{dt} = \frac{dH}{dT} \cdot \frac{dT}{dt} = C_p(T) \cdot R \quad (3)$$

According to Eq. 4, $C_p(T)$ can be directly measured by division of power to the rate of heating which for a semi-crystalline polymer is shown schematically in Fig. 2.

$$C_p(T) = \frac{P(t)}{R} \quad (4)$$

The heat capacity of the sample in different states can be defined as follows: below T_g where the amorphous and crystalline regions exist in semi-crystalline materials, the specific heat capacity can be calculated by Eq. 5 where Φ_k is the fraction of crystalline, accordingly $(1 - \Phi_k)$ is the fraction of amorphous glassy state. The parameters, $C_{p,k}$ and $C_{p,g}$, are, respectively, the heat capacity of the crystalline and glassy of the partially melted material. In region II, between T_g and T_m^0 , C_p is defined as Eq. 5:

$$C_p = \phi_k \cdot C_{p,k} + (1 - \phi_k) \cdot C_{p,g} \quad (5)$$

In region III, where the entire material has melted and is in the liquid state, C_p is defined as $C_{p,l}$. In practice, the melting transition spreads out as a Gaussian distribution trace due to the distribution of crystal size or lamellar domains giving rise to a melting point distribution, notated as $\rho(T)$. The latent heat of melting is driven by the transition of the crystalline state to the liquid state which therefore is $(1 - \Phi_k) \cdot \Delta H_m$.

The total heat capacity of a melted material is the summation of the heat capacity in the three regions, namely below (I), during (II), and above the melting transition or region (III) which is represented in Eq. 6:

$$C_p(T) = \frac{P(T)}{R} = \frac{dH}{dT} = C_{p,k} + (C_{p,l} - C_{p,k}) \cdot \int_0^T \rho(T) dT \quad (6)$$

The normalized heat flow at a given temperature in the DSC endothermic curve is proportional to the mass fraction of the molten crystals at that temperature [14]. The crystal size distribution $\rho(T)$ can be derived from the Arrhenius function¹ (Eq. 7) which is linearized around the equilibrium melting point (T_m^0).

$$K = A \cdot e^{-E_a/RT} \quad (7)$$

The crystal size distribution, $\rho(T)$, is calculated by defining the Arrhenius Equation around T_m^0 with a small ΔT , the melting point distribution, where E_a is the activation energy of the T which is dependent of the viscosity around T_m^0 (Eq. 8).

$$\rho(T) = e^{E_a/RT_m^0} \cdot e^{-E_a/RT} \quad (8)$$

Here, $\frac{E_a}{R}$ is the activation energy of the process per mole; therefore, $e^{\frac{E_a}{R}}$ is a large constant value, notated as A , where linearizing around T_m^0 and $\alpha = \frac{E_a}{R \cdot (T_m^0)^2}$ with the unit of (K^{-1}) solves Eq. 9 to give Eq. 10:

$$\rho(T) = e^{\alpha \Delta T} \quad (9)$$

The crystal size distribution, $\rho(T)$, calculated based on Eq. 10 is not the normalized surface area since the area under the melting transition is associated to the crystalline fraction of the material; therefore, $\int \rho(T) \cdot dT = 1$. The surface under the melting transition trace (Z) is calculated by Eq. 10 as follows:

¹ Arrhenius function describes the dependence of the rate constant of a chemical reaction or physical transition on the absolute temperature (Eq. 7) where K is the rate constant, T is the absolute temperature (Kelvins), A is the pre-exponential factor, E_a is the activation energy for the reaction (in the same units as RT), and R is the universal gas constant).

$$Z = \int_0^{\infty} e^{\alpha x} \cdot dx = \frac{1}{\alpha} e^{\alpha x} \Big|_{-\infty}^0 = \frac{1}{\alpha} \quad (10)$$

The normalized $\rho(T)$ around T_m^0 where $\Delta T \leq 0$ is given in Eq. 11 which yields in Eq. 12 where $\alpha = \frac{T_a}{T_m^0}$ and the activation temperature is denoted as $T_a = \frac{E_a}{k}$.

$$\rho(T) = \rho(T_m^0 + \Delta T) = e^{\alpha \Delta T} \quad (11)$$

$$\rho_N(T) = \frac{1}{\alpha} \cdot e^{\alpha \Delta T} \quad (12)$$

The limited resolution of a DSC instrument and difference in the thermal conductivity, for example in the case of organic compounds, could cause a non-isothermal measurement which leads to a Gaussian distribution of the heat flow versus temperature where impurities may also influence the sharpness of the transition peak which gives

$$DSC_N(T) = \Delta H \cdot \frac{\alpha}{2} \cdot e^{\frac{\alpha^2}{4\beta}} \cdot e^{\alpha(T-T_m^0)} \cdot \text{erfc} \left(\sqrt{\beta} (T - T_m^0 + \frac{\alpha}{2\beta}) \right) + \Delta C_{p,m} \cdot \frac{1}{2} \cdot e^{\frac{-\alpha^2}{4\beta}} \cdot \left(e^{\frac{\alpha^2}{2\beta}} \cdot e^{\alpha(T-T_m^0)} \cdot \text{erfc} \left(\sqrt{\beta} (T - T_m^0 + \frac{\alpha}{2\beta}) \right) + e^{\frac{\alpha^2}{4\beta}} \cdot \left(\text{erf} \sqrt{\beta} (T - T_m^0) \right) + 1 \right)$$

$$\Delta C_p(T) = \Delta C_{p,m} \cdot \frac{1}{2} \cdot e^{\frac{-\alpha^2}{4\beta}} \cdot \left(e^{\frac{\alpha^2}{2\beta}} \cdot e^{\alpha(T-T_m^0)} \cdot \text{erfc} \left(\sqrt{\beta} (T - T_m^0 + \frac{\alpha}{2\beta}) \right) + e^{\frac{\alpha^2}{4\beta}} \cdot \left(\text{erf} \left(\sqrt{\beta} (T - T_m^0) \right) \right) + 1 \right) \quad (19)$$

rise to the additional broadening in Gaussian distribution explained by $\rho(T)$. The Gaussian function, $f_N(\Delta T)$, taking the broadening effect into account is defined as Eq. 13.

$$f_N(\Delta T) = \frac{1}{\sigma \sqrt{2\pi}} \cdot e^{-\frac{1}{2} \left(\frac{\Delta T}{\sigma} \right)^2} \quad (13)$$

The convolution of $\rho_N(T)$ and $f_N(\Delta T)$ expressing how the shape of one function is modified by the other produces a third function defined as the integral of the product of the two functions after one is reversed and shifted. Therefore, the integral is evaluated for all values of the shift, producing the convolution function (Eq. 14).

$$DSC_N(\Delta T) = \rho_N(T) * f_N(\Delta T) = \int_{-\infty}^0 \rho(p) f(\Delta T - p) \cdot dp \quad (14)$$

$$DSC(T) = \frac{A}{2\alpha} \cdot e^{\alpha(T-T_m^0)} \cdot \text{erfc} \left(\sqrt{\beta} (T - T_m^0 + \frac{\alpha}{2\beta}) \right) \quad (15)$$

The normalization by dividing by $\frac{A}{2} \cdot e^{\frac{\alpha^2}{4\beta}}$ gives $\Delta H = \frac{A}{\alpha^2} \cdot e^{-\frac{\alpha^2}{4\beta}}$ which with Eq. 15 yields Eq. 16:

$$DSC(T) = \frac{\alpha}{2} \cdot e^{\frac{\alpha^2}{4\beta}} \cdot \left(e^{\alpha(T-T_m^0)} \cdot \text{erfc} \left(\sqrt{\beta} (T - T_m^0 + \frac{\alpha}{2\beta}) \right) \right) \quad (16)$$

The DSC(T) in Eq. 16 requires to be normalized, regardless of the peak shape, the total energy required to melt the same amount of material remains constant, i.e., the area under the melting trace is constant. Therefore, the total energy to melt the material, ΔH , which is obtained by integration of the DSC trace, is equal to 1 $(\int_{-\infty}^{\infty} \frac{\alpha}{2} \cdot e^{\frac{\alpha^2}{4\beta}} \cdot \left(e^{\alpha(T-T_m^0)} \cdot \text{erfc} \left(\sqrt{\beta} (T - T_m^0 + \frac{\alpha}{2\beta}) \right) \right) = 1)$. By changing the variables as $z = \Delta T + \frac{\alpha}{2\beta}$ thus, $\Delta T = z - \frac{\alpha}{2\beta}$ and solving the integration, the cumulative function is obtained by Eq. 17:

$$H(z) = \frac{\alpha}{2} \cdot e^{\frac{\alpha^2}{4\beta}} \cdot \frac{1}{\alpha} \cdot \left(e^{\alpha z} \cdot \text{erfc}(\sqrt{\beta} \cdot z) + e^{\frac{\alpha^2}{4\beta}} \cdot \left(\text{erf} \left(\sqrt{\beta} \left(z - \frac{\alpha}{2\beta} \right) \right) + 1 \right) \right) \quad (17)$$

Changing the variables with the original notations yields Eq. 18 where the second term represents $\Delta C_{p,m}(T)$ which can be given in the separate equation, Eq. 19:

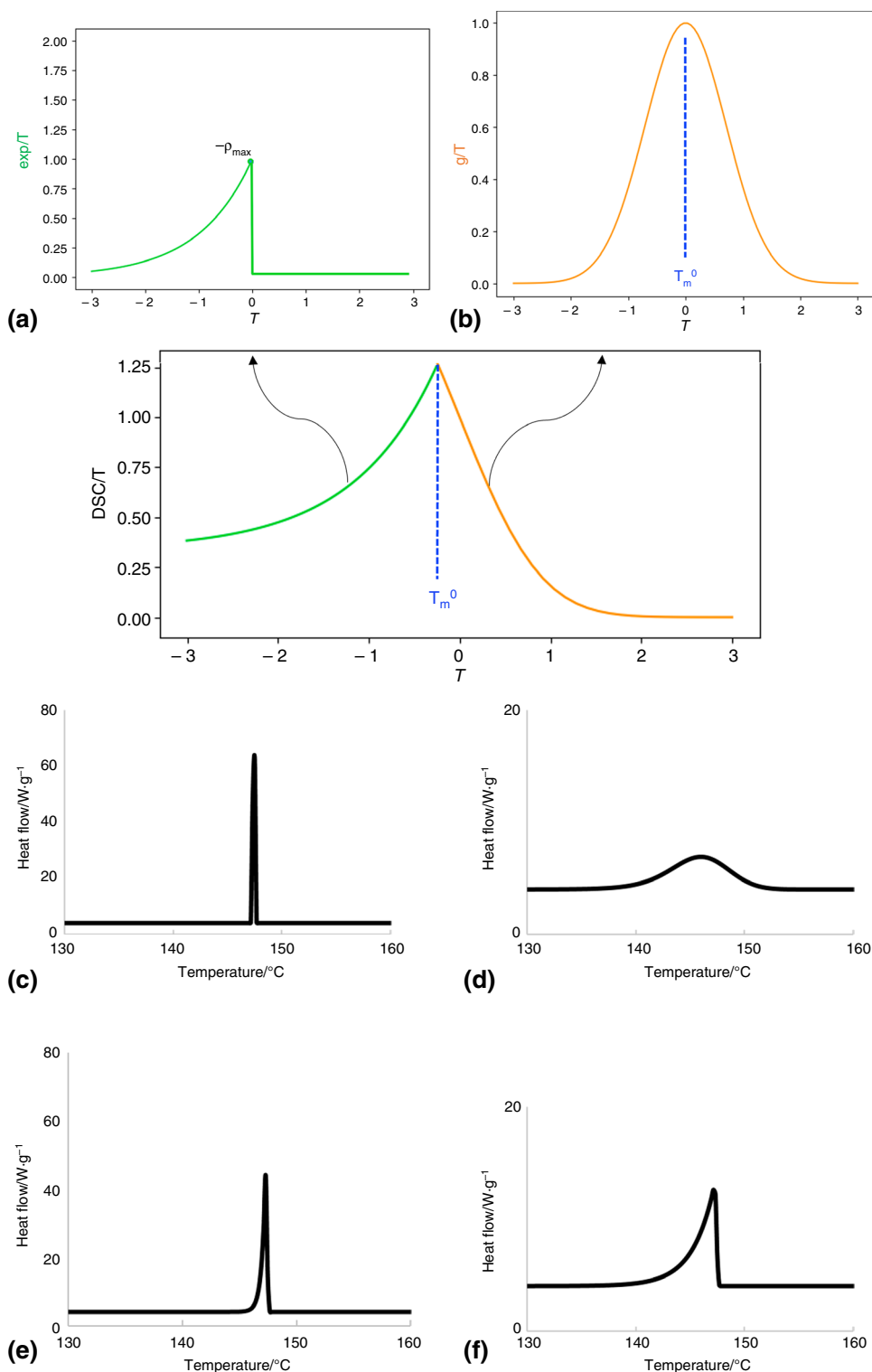
$$\quad (18)$$

Adding functions to adjust the fit for baseline and its shifting level gives rise to the equation below:

$$DSC_N(T) = \Delta H \cdot \frac{\alpha}{2} \cdot e^{\frac{\alpha^2}{4\beta}} \cdot e^{\alpha(T-T_m^0)} \cdot \text{erfc} \left(\sqrt{\beta} (T - T_m^0 + \frac{\alpha}{2\beta}) \right) + \Delta C_p(T) + B + C(T - T_m^0) + D(T - T_m^0)^2 \quad (20)$$

The analytical function (Eq. 20) formulates the heat flow of the DSC trace for melting transition and extends to the other phenomena such as crystallization, glass transition, liquid-crystal phase transitions to calculate the equilibrium transition temperature. The equilibrium melting temperature, T_m^0 , can be calculated by this function for crystals with infinite size irrespective of how fast or how slow the crystallites crystallize or melt. This function is based on two main functions: the convolution of the Arrhenius-like crystal size distribution function, $e^{\alpha(T-T_m^0)}$, and the Gaussian peak broadening ($e^{\alpha(T-T_m^0)}$) as shown in Fig. 3. The Arrhenius function can cause a negative skew at the low temperature side of the peak (negative asymmetry in peak shape) which is usually the case for a melting transition. Positive asymmetry can occur in the melting peak shape if there are serious thermal gradients caused by a (too) high rate of measurement or too

Fig. 3 Schematic underlying mathematics representing the convolution of the Analytical DSC function to two main functions and the effect of α and β on the peak shape, symmetry and width; (a) the Arrhenius function ($\Delta T < 0$: $\rho(T)$), (b) the first-order guess of a step-wised function, complementary error function ($\Delta T > 0$: $\rho_{\max} \operatorname{erfc}(\Delta T/\omega)$), (c) symmetrical narrow peak by large α and β ($\alpha=50$, $\beta=100$), (d) symmetrical broad peak by small α and β ($\alpha=0.5$, $\beta=0.1$), (e) asymmetrical narrow peak by small α and large β ($\alpha=5$, $\beta=100$), (f) asymmetrical broad peak by small α and large β ($\alpha=0.5$, $\beta=50$)



thick sample. Positive asymmetry might also be observed upon crystallization and from thermal decomposition processes; however, this is outside the scope of this manuscript.

The α and β parameters are inversely proportional to the width of the peak; therefore, they determine the peak shape

in terms of the width and the asymmetry as shown schematically in Fig. 3c–f. The mathematical terms and physical attributions of the fit parameters of $\text{DSC}_N(T)$ are summarized in Table 1.

Table 1 The variables, functions, and the parameters of the $DSC_N(T)$

parameters	Power units	Thermodynamic units	Physical attributions and mathematical terms
T_m^0	°C	K	The equilibrium melting point of the phase transition
B	$W g^{-1}$	$J g^{-1} K^{-1}$	Baseline offset
C	$W g^{-1} K^{-1}$	$J g^{-1} s^{-1}$	Linear baseline slope
D	$W g^{-1} K^{-2}$	$J g^{-1} s^{-1} K^{-2}$	Second order baseline curvature
α	K^{-1}	K^{-1}	Strength of the linearized Arrhenius function ($\alpha = E_a/(R.(T_m^0)^2)$) describing the crystal size distribution, roughly proportional to the steepness of the rising edge of the peak
β	K^{-2}	K^{-2}	The parameter in relation to the Gaussian distribution of the peak ($\beta = \frac{1}{2\sigma^2}$), describing the peak broadening in the declining edge
$\Delta C_{p,m}$	$W g^{-1} K^{-1}$	$J K^{-1}$	The difference between the heat capacity of the solid and liquid state
$e^{\alpha(T-T_m^0)}$	–	–	The Arrhenius function determining the rising edge of the curve
$erfc\left(\sqrt{\beta}(T - T_m^0 + \frac{\alpha}{2\beta})\right)$	–	–	Erfc, the complementary error function, describes the falling edge of the peak as it returns to the baseline
ΔH	$W g^{-1}$	$J g^{-1}$	The coefficient of the $DSC_N(T)$ function representing the change in enthalpy associated with the phase transition
R^2	–	–	The statistical measure for the goodness of fit in a regression function that determines the amount of variance in the dependent variable that can be explained by the independent variable

Table 2 Experimental versus fit errors obtained by measuring DSC traces of 3 samples of the same Benzoic acid under the same condition and analyzed using Pyris software and fitting of $DSC_N(T)$ to the raw data, NA stands for not available

Characteristic parameters	From the literature measured with DSC [20]	From the experiment analyzed with Pyris	From the experiment analyzed with DSC_N/T	Fitting deviation (residuals of NLLS)
$\Delta H/J g^{-1}$	141.6	127.94 ± 2.39	147.50 ± 1.86	147.5022 ± 0.0018
$T_m^0/^\circ C$	121.4	122.23 ± 0.06	123.51 ± 0.07	123.5146 ± 0.0002
α/K^{-1}	NA	NA	1.95 ± 0.18	1.9595 ± 0.0009
β/K^{-2}			10.84 ± 4.18	10.8491 ± 0.0529
$\Delta C_{p,m}/W g^{-1} K^{-1}$			0.12 ± 0.03	0.1184 ± 0.0006
$B/W g^{-1}$			0.32 ± 0.13	0.3242 ± 0.0003
$C/W g^{-1} K^{-1}$			0.00 ± 0.00	-0.0007 ± 1.3804
$D/W g^{-1} K^{-2}$			0.00 ± 0.00	$(2.83 \pm 1.27) \times 10^{-5}$

The part of the DSC trace in pre- and post-transition, where no change occurs in the heat flow, is defined as the baseline (Fig. 1). According to Eq. 7, at the end of the melting transition, the whole $C_p(T)$ term turns into $(C_{p,l} - C_{p,k})$ which is the summation of heat capacity during the transition and the post-transition in the liquid state. Above the melting transition in the DSC of heat flow versus temperature, where the melting of all crystals has completed ($\rho(T)=0$), if the heat capacity of the solid and liquid state are equal ($\Delta C_p = C_{p,l} - C_{p,k} = 0$), the baseline becomes a horizontal flat line. As highlighted in Eq. 19, in $DSC_N(T)$, $\Delta C_{p,m}$ as one of the fit parameters can be fitted (Table 1) and absolute C_p is very inaccurate. For transitions where $\Delta C_p > 1$ or $\Delta C_p < 1$, the baseline steps up or down, respectively. This step has been defined in the function by the partial adjustment of the

slope which smoothly changes from pre- to post-transition, depending on how far the melting transition develops. In fact, $\int_0^T \rho(T)dT$ is the partial melting point which indicates that how much solid is still present in the system by subtracting the amount of the molten compound. On top of this theoretical equation, there is an instrumental calibration-related linear slope in the baseline or a quadratic curvature of the baseline.

Experimental error and fitting residuals

To extract accurate information from a raw DSC trace, three samples with nearly identical mass from the identical benzoic acid were heated under the same condition. The standard deviation of characteristic thermal properties such as T_m^0 and

Fig. 4 DSC of indium during heating from 25 to 170 °C at different scanning rates and $DSC_N(T)$ function fitted to the measured curves which were calibrated at the onset for the given rate, the heat flow has been normalized per mass of each sample, the unit of heat flow in each trace is ($W g^{-1}$)

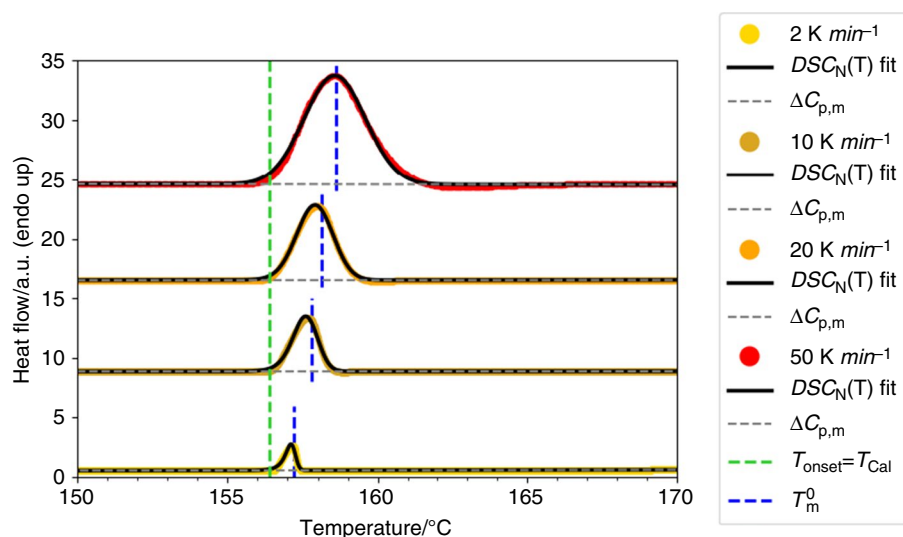


Table 3 Fit parameters of the $DSC_N(T)$ for experimental curves of indium (7 mg) heated at different rates after calibration for the given mass (the error margins are from the nonlinear fitting), *nonlinear

least squares error out of the bounds due to indeterminate high α value, NA stands for not available

Indium	Literature values [22]	R=2 K min ⁻¹	R=10 K min ⁻¹	R=20 K min ⁻¹	R=50 K min ⁻¹
$\Delta H/J g^{-1}$	28.51	30.15 ± 0.00	29.37 ± 0.01	28.62 ± 0.01	27.98 ± 0.04
$T_m^0/^\circ C$	156.60	157.22 ± 0.00	157.81 ± 0.00	158.11 ± 0.00	158.62 ± 0.61
α/K^{-1}	NA	4.88 ± 0.01	3.50 ± 0.03	4.44 ± 0.08	19.67^*
β/K^{-2}		37.44 ± 0.14	4.01 ± 0.02	1.54 ± 0.01	0.48 ± 0.03
$\Delta C_{p,m}/W g^{-1} K^{-1}$		0.01 ± 0.00	0.01 ± 0.00	-0.02 ± 0.00	0.00 ± 0.00

ΔH was obtained once by averaging the values from the raw data analyzed with the Pyris analyzer software which contains the experimental error and graphical examination error, depending on the selected temperature range. The standard deviation of function parameters was obtained by fitting the analytical model $DSC_N(T)$ to the three sets of raw data which contains the experimental error along with the fitting procedure error (Table 2). The fitting deviation for each parameter was obtained from the residuals of NLLS. The reported error margins of the fit parameters in this study are the residuals of NLLS rounded to two digits.

Validation of the analytical method for different types of materials

Indium as a metal calibration sample

To check the validity of the $DSC_N(T)$, the function was fitted to the experimental DSC curves of indium measured at different mass and heating rates. The traces in Fig. 4 were measured by heating from 25 to 170 °C at different scanning rates after the temperature and heat calibration for each given condition and normalization per mass of the sample.

As it is seen in Fig. 4, the onset has remained constant due to the calibration of the melting temperature defined at the onset of the peak. However, upon increasing the rate of heating the peak and endset values shift to higher temperatures due to the non-isothermal heating at high rates which is a well-known feature of a DSC [21].

The analytical function $DSC_N(T)$ has been fitted to the normalized experimental curves with a good correlation coefficients ($R^2 > 0.99$) for all rates (Table S1). The T_m^0 obtained from $DSC_N(T)$ is 157.22 ± 0.00 °C which shifts to 158.62 ± 0.61 °C upon increasing the heating rate from 2 to 50 K min⁻¹ due to the superimposition of the fit on the shifting peak (Table 3). At lower rates where the sample is at a better thermal equilibrium, T_m^0 obtained from the model, 157.22 ± 0.00 °C, is within less than 1 °C different from 156.59 °C reported by National Institute of Standards and Technology (NIST) for indium [22].

In the case of indium, the melting peaks measured at the all heating rates are symmetric. The width of the peak in the rising edge has been captured by α which decreases upon increasing the rate. In fact, α is in linear relationship with the activation energy (E_a), depending on the rate and mass of the sample [23]. The value of E_a determines the temperature

Fig. 5 DSC of different mass of indium measured with heating from 25 to 170 °C at 2 K min⁻¹ and DSC_N(T) function fitted to the experimental curves calibrated at the onset for the given mass, the heat flow has been normalized per mass of each sample, the unit of heat flow in each trace is (W g⁻¹)

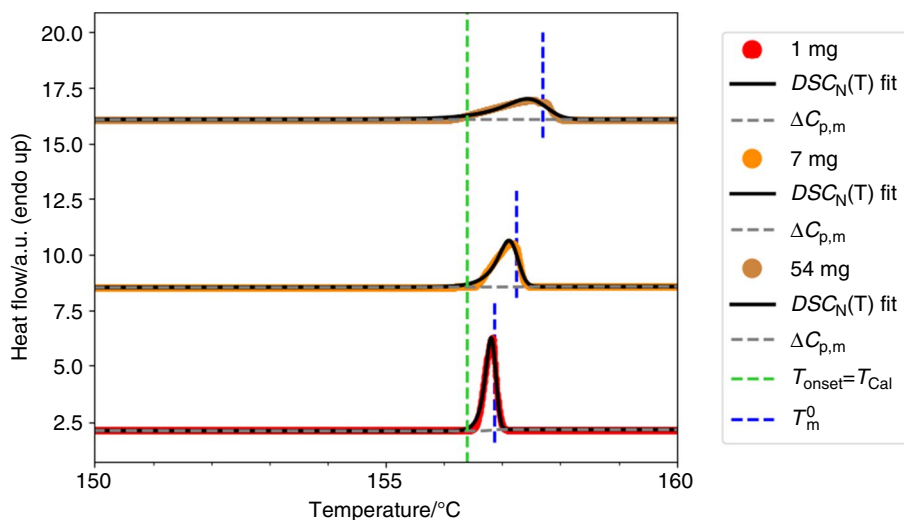


Table 4 Fit parameters of the DSC_N(T) for experimental curves of indium with different mass heated at 2 K.min⁻¹ measured after calibration at the onset for the given mass (the error margins are from the nonlinear fitting), NA stands for not available

Indium	Literature values [22]	m = 1 mg	m = 7 mg	m = 54 mg
$\Delta H/J \text{ g}^{-1}$	28.51	29.61 ± 0.00	30.27 ± 0.00	29.71 ± 0.00
$T_m^0/^\circ\text{C}$	156.60	156.86 ± 0.00	157.24 ± 0.00	157.69 ± 0.00
α/K^{-1}	NA	10.25 ± 0.03	4.43 ± 0.01	1.87 ± 0.00
β/K^{-2}		98.60 ± 0.27	34.49 ± 0.11	8.34 ± 0.03
$\Delta C_{p,m}/\text{W g}^{-1} \text{ K}^{-1}$		0.06 ± 0.00	0.01 ± 0.00	0.00 ± 0.00

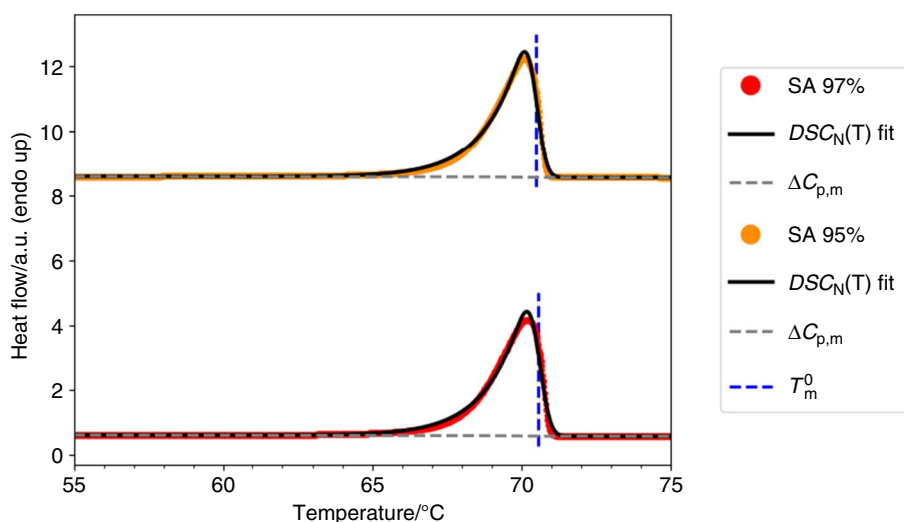
sensitivity of the melting transition; the higher the α and the larger the E_a become, the stronger the melting rate changes per the same change in temperature, and thus the steeper the slope of the rising edge becomes [24]. Although indium has a relatively good thermal conductivity, β decreases by increasing the heating rate; consequently, the peaks become broader. The peak area gets larger due to the peak broadening and the incorporated heating rate in the heat flow, which is measured by the DSC instrument as power (mW) (Eq. 3). The change in enthalpy of the fusion of indium varies from $27.98 \pm 0.04 \text{ J g}^{-1}$ to $30.15 \pm 0.00 \text{ J g}^{-1}$ which is comparable with the reported value by NIST 28.66 J g^{-1} . The change in the heat capacity, $\Delta C_{p,m}$, at different rates has remained very close to zero as the baseline levels remains at the same level in pre- and post-transition states. Figure 5 presents the DSC curves measured and normalized per mass of the samples (W g^{-1}) for different sample mass 1–54 mg at the common heating rate of 2 K.min^{-1} which is slow enough to keep the sample at the thermal equilibrium. The detected melting peak for 1 mg sample is extremely sharp and symmetric which turn to an asymmetric broad peak for the 54 mg sample where an overload effect causes a non-isothermal heat regime.

Similar to the rate effect, the onset values have remained constant due to the calibration at the onset, while the peak and endset values have shifted toward the higher

temperatures due to the increase in the thermal resistance of the samples at larger mass. As thermal transfer is much better across the contact zone between the solid indium and the aluminum pan, initial partial melting occurs with the formation of an interface liquid layer with different thermal properties than the solid indium. Therefore, the higher the mass of indium sample, the higher the thickness of sample, the larger the thermal gradient and temperature lag between these two parts.

The DSC_N(T) fits the DSC experimental traces (Fig. 5) with a good correlation coefficients ($R^2 > 0.97$) for all rates (Table S2). T_m^0 obtained by fitting of the DSC_N(T) on the measurement with 1 mg of indium is $156.86 \pm 0.00 \text{ }^\circ\text{C}$, which is the closest to the melting point of indium reported by NIST. It slightly shifts to higher temperature for larger sample mass (Table 4). β decreases by increasing the mass of the sample due to the larger thermal gradient which makes the peak broader. Similarly, α decreases which leads to the decrease in the slope of the rising edge of the peak due to the higher thermal gradient caused by higher mass for 7 mg sample. Progressively, increasing the mass to 54 mg decreases the slope of the rising edge since α decreases due to the recrystallization of the molten crystals on the existing non-molten crystals which spreads the crystal size distribution. A dramatic increase in the width of the peak at 54 mg is indeed caused by the increase in the domain of erfc at

Fig. 6 DSC of 6 mg SA with different purities heated at 2 K min^{-1} and $\text{DSC}_N(\text{T})$ function fitted to the measured curves after calibration at the onset for the given mass and rate



the decaying edge, the decrease in β and α , manifesting the width of the peak in the rising edge. ΔH obtained from the function fitted to the trace of 1 mg indium is the closest to the reported enthalpy for indium by NIST. The change in heat capacity, $\Delta C_{p,m}$, is zero which is manifested in the same baseline level of pre- and post-transition tails (Table 4).

Stearic acid as an organic compound

The DSC traces of 6 mg of stearic acid (SA) with two different purities (95% and 97%) were measured at 2 K min^{-1} after calibration of indium for the given rate and sample mass (Fig. 6).

The $\text{DSC}_N(\text{T})$ fits well to the both heating curves, $R^2 = 0.99$ (Table S5). T_m^0 obtained from the function is $70.5 \text{ }^\circ\text{C}$ for both samples () which is in a good agreement with the reported T_m^0 [25]. The temperature shifts to the lower temperatures due to the presence of impurity. This shift is not significant enough to be detected by the DSC instrument due to its low resolution. However, it has affected the β values relating to the peak width; β increases for the SA (97%) which has shown the less broad peak (Fig. 6). Compared to indium trace measured for nearly the same rate and mass, β of SA samples ($\beta_{\text{SA } 95\%} = 6.08 \pm 0.07 \text{ K}^{-2}$ and $\beta_{\text{SA } 97\%} = 7.05 \pm 0.08 \text{ K}^{-2}$) are significantly smaller than β of indium ($\beta_{\text{indium}} = 34.49 \pm 0.11 \text{ K}^{-2}$). As a result, the melting peaks of SA samples have become more asymmetric and broader at the declining edge of the peak due to its relatively lower thermal conductivity. Despite β , α has not changed significantly (Table 5); in fact, the presence of more impurity could lead to the faster crystallization

but not necessarily narrower crystal size distribution. The latent heat obtained from $\text{DSC}_N(\text{T})$ for SA (95%) and SA (97%) is in good agreement with the enthalpy of fusion of SA measured with DSC at 10 K min^{-1} by Xu et al. [26]. The deviation can be due to the weighing accuracy. The negative $\Delta C_{p,m}$ for both samples ($-0.02 \pm 0.00 \text{ W g}^{-1} \text{ K}^{-1}$) indicates the step-down in the baseline moving from pre- to the post-transition tail.

Phase transitions in a liquid crystal compound

Three endothermic peaks were observed in the DSC experimental trace of 8OCB (4'-octyloxy-4-cyanobiphenyl) heated from 0 to $100 \text{ }^\circ\text{C}$ at 2 K min^{-1} (Fig. 7).

The $\text{DSC}_N(\text{T})$ function fits to the first and third transition peaks with asymmetric shape very well ($R^2 > 0.99$) and ($R^2 = 0.97$) respectively (Table S6). The obtained temperature of each transition, T_m^0 , for these peaks is, respectively, at $55.62 \pm 0.00 \text{ }^\circ\text{C}$, $66.96 \pm 0.00 \text{ }^\circ\text{C}$, and $80.16 \pm 0.00 \text{ }^\circ\text{C}$ which could be attributed to the transitions

Table 5 Fit parameters of the $\text{DSC}_N(\text{T})$ fitted to the experimental curves of stearic acid (SA) with different degrees of impurities heated at 2 K min^{-1} after calibration at the onset for the given mass and rate, NA stands for not available

Stearic acid/SA	Literature values	SA 95%	SA 97%
$\Delta H/J \text{ g}^{-1}$	216.5 [25]	215.73 ± 0.01	213.99 ± 0.01
$T_m^0/^\circ\text{C}$	69.3 [26]	70.57 ± 0.00	70.48 ± 0.00
α/K^{-1}	NA	0.82 ± 0.00	0.81 ± 0.00
β/K^{-2}		6.08 ± 0.07	7.05 ± 0.08
$\Delta C_{p,m}/\text{W g}^{-1} \text{ K}^{-1}$		-0.02 ± 0.00	-0.02 ± 0.00

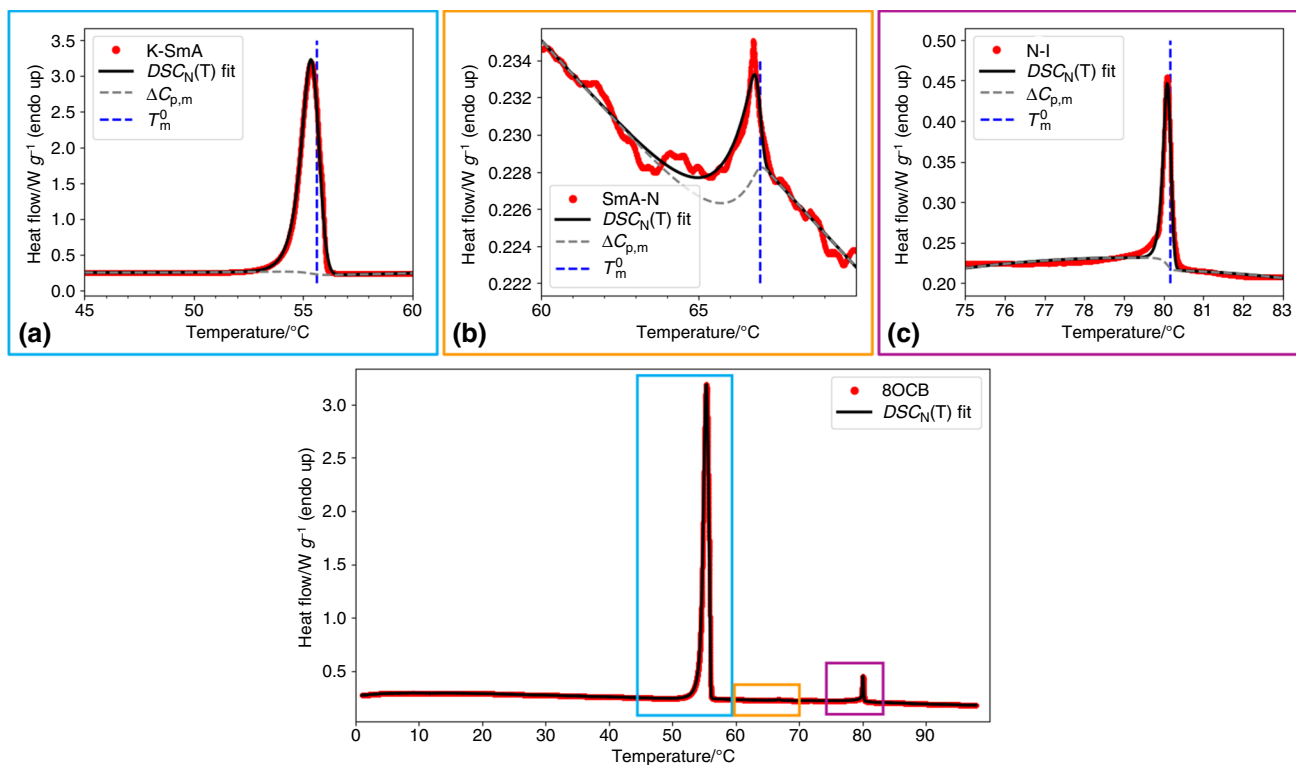


Fig. 7 DSC of 8OCB and $DSC_N(T)$ function fitted to the measured curves for 6 mg of 8OCB heated at $2 \text{ K}\cdot\text{min}^{-1}$ after calibration for the given mass and rate, $\Delta C_{p,i}$ is the change in heat capacity for different liquid crystal transitions: (a) K to Sm-A, (b) Sm-A to N, and (c) N to I

Table 6 Fit parameters of the $DSC_N(T)$ for experimental curves of 6 mg of 8OCB (4'-octyloxy-4-cyanobiphenyl) heated at $2 \text{ K}\cdot\text{min}^{-1}$ after temperature calibration of indium at the onset for the given mass and rate (the error margins are from the nonlinear fitting)

8OCB	1st peak/K-SmA	2nd peak/SmA-N	3rd peak/N-I
$\Delta H/J \text{ g}^{-1}$	97.05 ± 0.00	0.21 ± 0.00	1.74 ± 0.00
Literature $\Delta H/J \text{ g}^{-1}$	140.32 [28]	0.9 ± 0.9 [29]	1.55 ± 0.05 [29]
$T_m^0/^\circ\text{C}$	55.62 ± 0.00	66.96 ± 0.00	80.16 ± 0.00
Literature $T_m^0/^\circ\text{C}$	53.54 [28]	65.25 [28]	78.53 [28]
α/K^{-1}	2.31 ± 0.00	1.01 ± 0.01	10.36 ± 0.12
β/K^{-2}	5.72 ± 0.02	36.21 ± 2.16	91.10 ± 1.15
$\Delta C_{p,i}/\text{W g}^{-1} \text{ K}^{-1}$	-0.06 ± 0.00	0.01 ± 0.00	-0.01 ± 0.00

from crystalline to Smectic-A phase (K-SmA) at $53.54 \text{ }^\circ\text{C}$, Smectic-A to Nematic (SmA-N) at $65.25 \text{ }^\circ\text{C}$, and Nematic to isotropic (N-I) at $78.53 \text{ }^\circ\text{C}$, respectively (Table 6). The enthalpy change of these transitions was obtained from the $DSC_N(T)$, which was in good agreement with the values reported in the literature [27–29]. The difference in the obtained enthalpy change and the reported values is due to different calibration approaches, setting peak value instead of the onset value.

Low molecular mass bisamide gelators with different number of methylene spacers between the amide groups

As Fig. 8 shows, the melting peaks of bisamide low molecular mass gelators, briefly nBA where n represents the odd and even spacer length between the amide groups, were observed upon heating at $10 \text{ K}\cdot\text{min}^{-1}$. $DSC_N(T)$ function fits remarkably well on the experimental traces of all these nBA compounds, $R^2 > 0.98$ (Table S7).

Fig. 8 DSC experimental traces and $DSC_N(T)$ function fitted to the measured curves of nBA compounds (6 mg) heated at 10 K min^{-1} after temperature calibration of indium at the onset for the given mass and rate

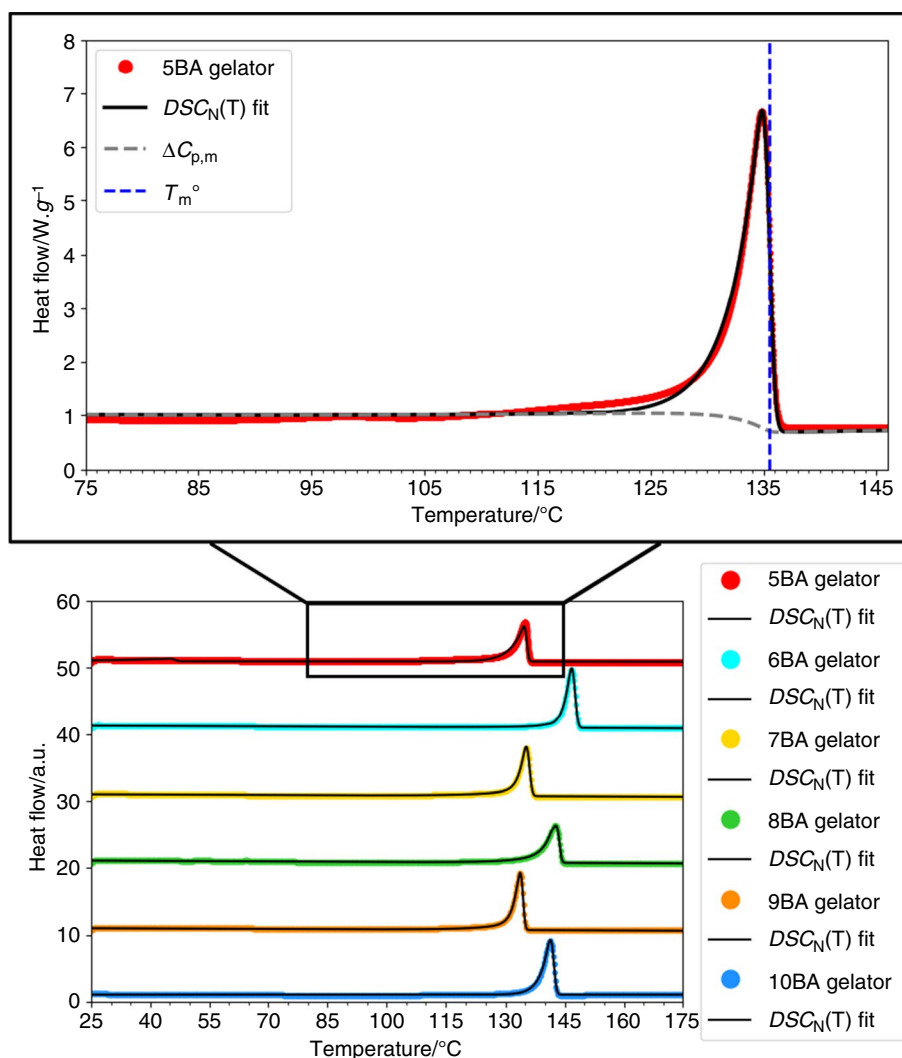


Table 7 Fit parameters of the $DSC_N(T)$ for experimental curves of 6 mg of odd and even bisamides heated at 10 K.min^{-1} after calibration at the onset for the given mass and rate (the error margins are

from the nonlinear fitting) and calculated T_m and ΔH from Pyris analyzing software, these compounds were newly synthesized, and there are no data available in the literature for comparison

nBA	5BA	6BA	7BA	8BA	9BA	10BA
$\Delta H/J\text{ g}^{-1}$ from $DSC_N(T)$	126.18 ± 0.04	168.66 ± 0.07	140.88 ± 0.09	155.12 ± 0.12	149.21 ± 0.08	172.20 ± 0.06
$\Delta H/J\text{ g}^{-1}$ from Pyris	100.2 ± 5.7	117.6 ± 2.5	113.1 ± 6.3	123.1 ± 3.4	118.4 ± 5.3	139.6 ± 2.6
$T_m^0/^\circ\text{C}$ from $DSC_N(T)$	135.52 ± 0.00	147.46 ± 0.00	135.97 ± 0.00	143.53 ± 0.00	132.50 ± 0.00	142.11 ± 0.00
$T_m/^\circ\text{C}$ from Pyris	135 ± 1	147 ± 1	135 ± 1	143 ± 1	134 ± 1	141 ± 1
α/K^{-1}	0.39 ± 0.00	0.63 ± 0.00	0.52 ± 0.00	0.31 ± 0.00	0.52 ± 0.00	0.48 ± 0.00
β/K^{-2}	3.01 ± 0.04	1.19 ± 0.02	1.50 ± 0.03	1.69 ± 0.04	2.68 ± 0.05	1.40 ± 0.02
$\Delta C_{p,m}/\text{W g}^{-1}\text{ K}^{-1}$	-0.44 ± 0.01	-0.31 ± 0.01	-0.40 ± 0.01	-0.28 ± 0.01	-0.35 ± 0.01	-0.29 ± 0.01

Fig. 9 (a) $DSC_N(T)$ function fitted to the experimental traces of 6 mg of molecularly mixed binary bisamides (blends of 5BA and 6BA in different molar ratios) heated at 10 K min^{-1} after calibration at the onset for the given sample mass and rate, (b) phase diagram of binary 5BA6BA, T_m^0 obtained from the $DSC_N(T)$ fitting the DSC traces of 5BA6BA blends at different molar ratios (the error bars from the nonlinear fitting are not visible since they are very small (Table S6)), (c) enthalpy change of individual phases in 5BA6BA and the total enthalpy change of the compounds at different ratios obtained from the $DSC_N(T)$ and plotted versus the mole fraction of 6BA in 5BA (the error bars from the nonlinear fitting are not visible since they are very small (Table S6)), the trend lines are to guide the eye

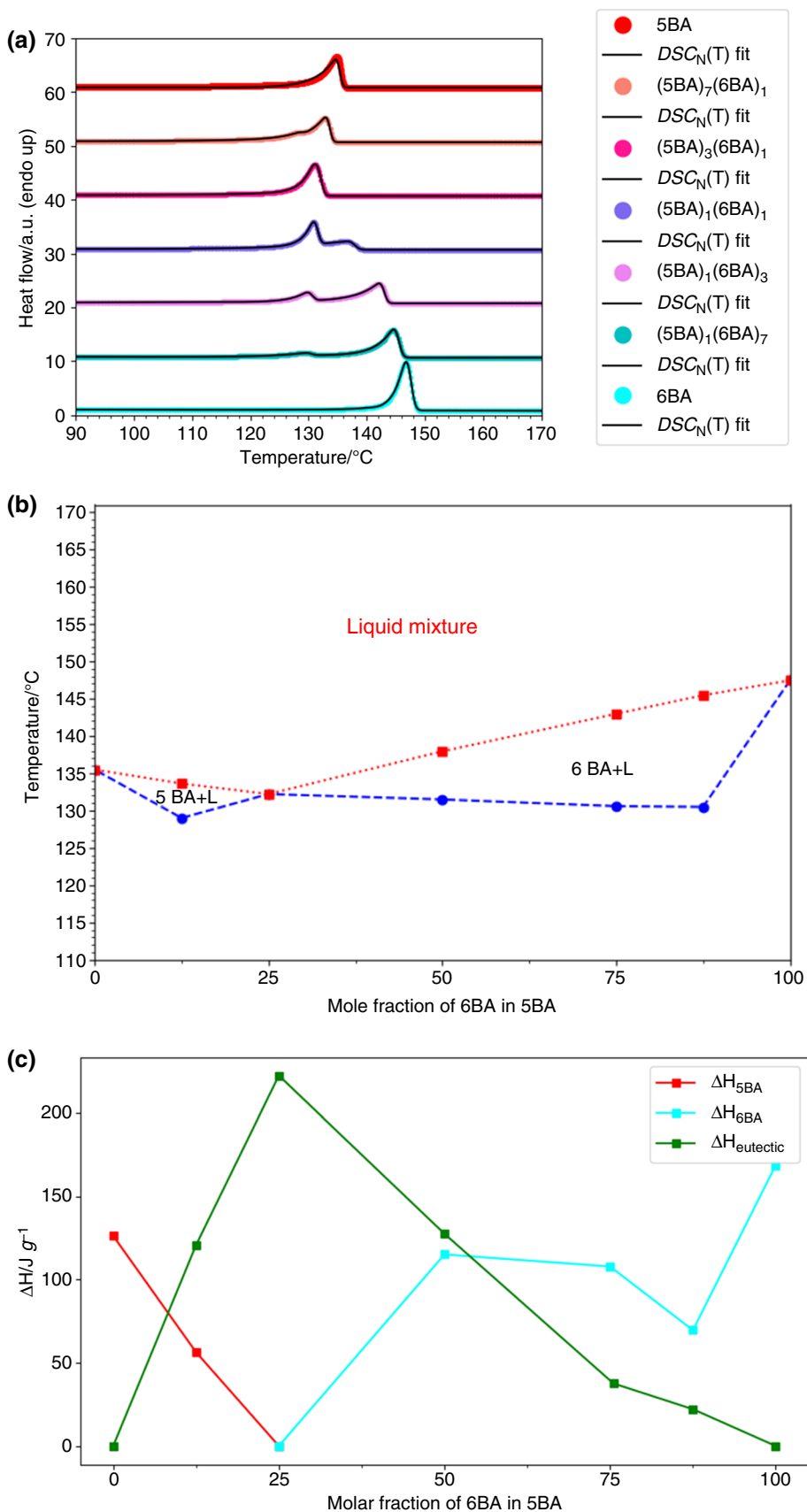


Table 8 Fit parameters of the $DSC_N(T)$ function fitted to the experimental DSC trace of 6 mg of molecularly mixed binary bisamides (5BA6BA in different ratios) heated at $10 \text{ K}\cdot\text{min}^{-1}$ after calibration at the onset for the given mass and rate, in the case of $(5BA)_3(6BA)_1$, only one fitting peak is required due to the peak overlap (the error

margins are from the nonlinear fitting), $\Delta C_{p,m}$ is not available (NA) due to purely mathematical artifact, if the peaks are sufficiently apart with sufficient baseline tail on each side, the cumulative $\Delta C_{p,m}$ can be reliably determined via the function

Binary 5BA6BA	6BA	$(5BA)_1(6BA)_7$	$(5BA)_1(6BA)_3$	$(5BA)_1(6BA)_1$	$(5BA)_3(6BA)_1$	$(5BA)_7(6BA)_1$	5BA
<i>First peak</i>							
$\Delta H_1/J \text{ g}^{-1}$	Single peak	22.08 ± 0.05	37.56 ± 0.03	69.54 ± 0.02	222.3 ± 7.07	56.34 ± 0.76	Single peak
$T_{m,1}^0/^\circ\text{C}$		130.49 ± 0.03	130.59 ± 0.00	131.49 ± 0.00	132.21 ± 0.02	129.00 ± 0.02	
α_1/K^{-1}		0.17 ± 0.00	0.38 ± 0.00	0.61 ± 0.00	0.07 ± 0.00	0.07 ± 0.00	
β_1/K^{-2}		1.20 ± 0.12	1.41 ± 0.04	1.94 ± 0.02	2.43 ± 0.28	1.62 ± 0.21	
$\Delta C_{p,m,1}/\text{W g}^{-1} \text{ K}^{-1}$	NA						
<i>Second peak</i>							
$\Delta H_2/J \text{ g}^{-1}$	168.66 ± 0.07	127.44 ± 0.06	107.76 ± 0.11	115.02 ± 0.12	Single peak	120.6 ± 0.23	126.18 ± 0.04
$T_{m,2}^0/^\circ\text{C}$	147.46 ± 0.00	145.46 ± 0.00	142.97 ± 0.00	137.94 ± 0.01		133.62 ± 0.00	135.49 ± 0.00
α_2/K^{-1}	0.63 ± 0.00	0.36 ± 0.00	0.27 ± 0.00	0.09 ± 0.00		0.30 ± 0.00	0.39 ± 0.00
β_2/K^{-2}	1.19 ± 0.02	1.50 ± 0.02	1.89 ± 0.03	1.11 ± 0.02		2.65 ± 0.04	3.01 ± 0.04
$\Delta C_{p,m,2}/\text{W g}^{-1} \text{ K}^{-1}$	NA						
R^2	0.99	0.99	0.99	0.99	0.99	0.99	0.99

T_m^0 and the ΔH of fusion for our newly synthesized bisamide compounds (Table 7) were obtained more reliably from the $DSC_N(T)$ than the analyzing software [6].

$\Delta C_{p,m}$ of all the traces are negative which shows a downward step in baseline from pre- to post-melting transition tail (Table 7). In crystals where the molecules are free to rattle in the crystal lattice, the heat capacity of the solid state will be higher than the heat capacity of the liquid state where the molecules cannot rattle anymore and they are sterically interacting. As a result, their freedom is lost to a great extent upon melting.

Binary systems (binary mixture of low molecular mass gelators)

The $DSC_N(T)$ for binary compounds can be obtained based on Eq. 21, where T_r is the reference temperature for the overall curved baseline.

$$\begin{aligned}
 DSC_N(T) = & \left(\Delta H_1 \cdot \frac{\alpha_1}{2} \cdot e^{\frac{\alpha_1^2}{4\beta_1}} \cdot e^{\alpha_1(T-T_{m,1}^0)} \cdot \text{erfc} \left(\sqrt{\beta_1} \left(T - T_{m,1}^0 + \frac{\alpha_1}{2\beta_1} \right) \right) + \Delta C_{p,1}(T) \right) \\
 & + \left(\Delta H_2 \cdot \frac{\alpha_2}{2} \cdot e^{\frac{\alpha_2^2}{4\beta_2}} \cdot e^{\alpha_2(T-T_{m,2}^0)} \cdot \text{erfc} \left(\sqrt{\beta_2} \left(T - T_{m,2}^0 + \frac{\alpha_2}{2\beta_2} \right) \right) + \Delta C_{p,2}(T) \right) \\
 & + B + C(T - T_r) + D(T - T_r)^2
 \end{aligned} \quad (21)$$

The $DSC_N(T)$ function fits to the heat flow curves of all binary mixtures of 5BA and 6BA in different ratios with $R^2 = 0.99$ (Table S8). As Fig. 9a shows, except for $(5BA)_3(6BA)_1$, two distinct melting peaks were observed

in the heating traces of all binary mixtures which indicates the tendency of these molecules for phase separation. T_m^0 and ΔH for all compounds were obtained reliably from $DSC_N(T)$. For the overlapping peaks $\Delta C_{p,m}$ does not converge due to purely mathematical artifact. However, if the peaks are sufficiently apart with sufficient baseline tail on each side, the cumulative $\Delta C_{p,m}$ can be reliably determined via fitting the function to the DSC trace.

As Fig. 9b shows, the phase diagram of 5BA6BA mixture is plotted using the accurate T_m^0 obtained for each phase from the fitting of $DSC_N(T)$ to the DSC traces of 5BA6BA (Table 8). The mixture with $(5BA)_3(6BA)_1$ composition shows a single melting transition with the lower melting point ($132.21 \pm 0.02 \text{ }^\circ\text{C}$) compared to single 5BA and 6BA compounds. The occurrence of the mixture at the

non-equimolar ratio can be due to the difference in H-bonding patterns of 5BA and 6BA compounds where 5BA has more freedom than 6BA to bond to an adjacent molecule [6]. The latent heat for each phase individually has been obtained from the $DSC_N(T)$ (Table 8). As shown in the

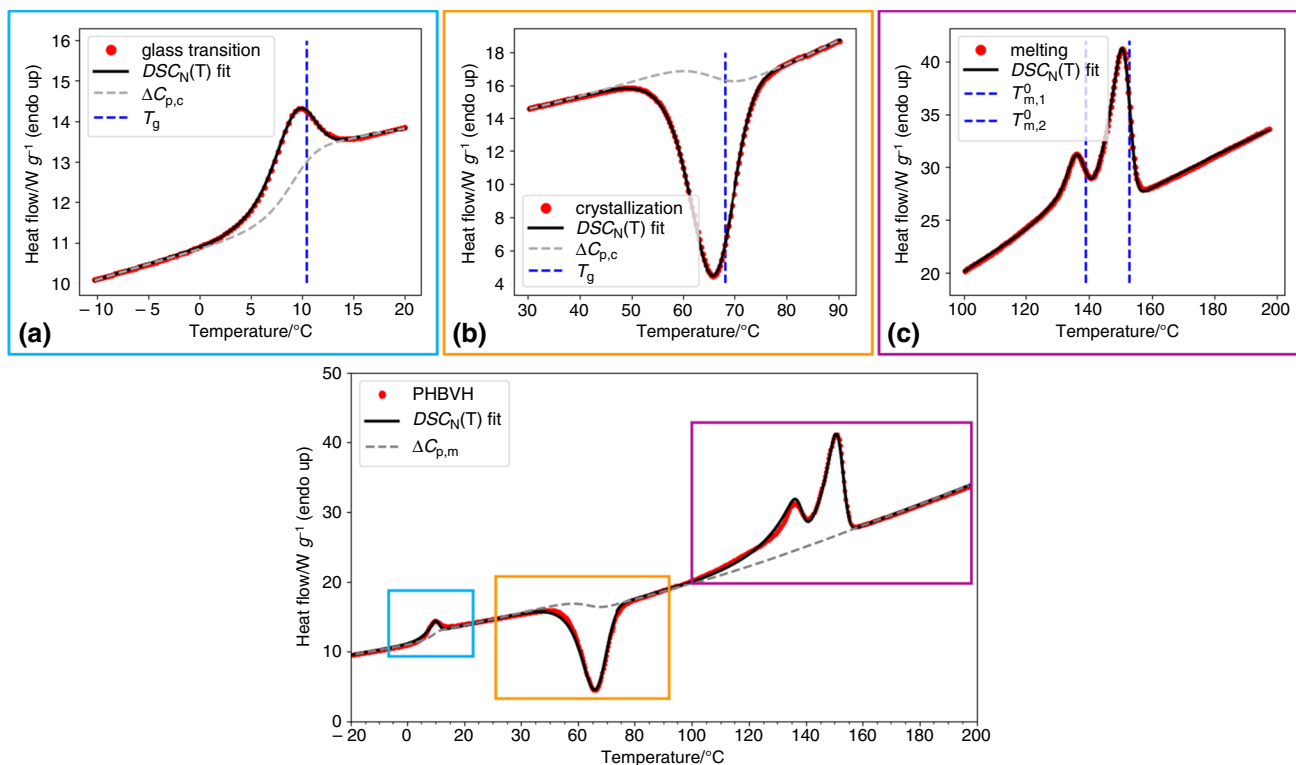


Fig. 10 $DSC_N(T)$ function fitted to the experimental traces of 6 mg of PHBVH heated after calibration at the onset for the given sample mass and rate. For the overlapping peaks, $\Delta C_{p,m}$ does not converge (not available = NA) due to purely mathematical artifact

Table 9 Fit parameters of the $DSC_N(T)$ for experimental curves of 6 mg of PHBVH after calibration at the onset for the given sample mass and rate (the error margins are from the nonlinear fitting), *nonlinear least squares error out of the bounds due to indeterminate high α value

PHBVH	1 st peak Glass transition/ T_g	2 nd peak Crystallization/ T_c	1 st melting peak/ $T_{m,1}^0$	2 nd melting peak/ $T_{m,2}^0$
$\Delta H/J\ g^{-1}$	13.54 ± 0.08	201.90 ± 0.24	75.57 ± 1.35	136.31 ± 0.75
$T_t^0/^\circ C$	10.45 ± 0.02	68.01 ± 0.01	138.88 ± 0.03	152.72 ± 0.01
α/K^{-1}	0.45 ± 0.01	0.28 ± 0.00	6.77*	0.02 ± 0.00
β/K^{-2}	0.23 ± 0.01	0.04 ± 0.00	0.08 ± 0.03	0.12 ± 0.00
$\Delta C_{p,t}/W\ g^{-1}\ K^{-1}$	1.82 ± 0.03	2.46 ± 0.04	NA	NA

enthalpy diagram (Fig. 9c), the mixture $(5BA)_3(6BA)_1$ has the highest latent heat ($222.3 \pm 7.07\ J\ g^{-1}$).

Semi-crystalline polymer (PHBVH) with glass transition, cold crystallization, and melting peaks

The DSC of PHBVH upon heating (Fig. 10) shows multiple transitions: a glass transition which is followed by a cold crystallization, the exothermic crystallization process which is observed on heating of a sample that has previously been cooled so quickly that has no time to crystallize. In fact, at temperature below the glass transition, the molecular mobility is restricted and cold crystallization does not occur, but

above the glass transition, small crystals are formed at relatively low temperatures. In addition, two endothermic peaks were observed subsequently upon further heating. The glass transition was fitted by $DSC_N(T)$ function (Eq. 20). The cold crystallization peak was fitted by using a negative ΔH as stated in Eq. 22. The melting transition peaks were fitted by $DSC_N(T)$ for binary peaks (Eq. 21). As Fig. 10 shows, $DSC_N(T)$ function fits all peaks remarkably well, $R^2 > 0.99$ (Table S9).

$$DSC_N(T) = -\Delta H \cdot \frac{\alpha}{2} \cdot e^{\frac{\alpha^2}{4\beta}} \cdot e^{\alpha(T-T_m^0)} \cdot \operatorname{erfc}\left(\sqrt{\beta}(T-T_m^0 \pm \frac{\alpha}{2\beta})\right) \pm \Delta C_{p,m}(T) \pm B \pm C(T-T_m^0) \pm D(T-T_m^0)^2 \quad (22)$$

The glass transition temperature, crystallization temperature, and melting points obtained from the corresponding $DSC_N(T)$ are $T_g^0 = 10.45 \pm 0.02$ °C, $T_c^0 = 68.01 \pm 0.01$ °C, and $T_{m,1}^0 = 138.88 \pm 0.03$ °C and $T_{m,2}^0 = 152.72 \pm 0.01$ °C [30, 31]. For the glass transition and melting transitions, the baselines step up from the pre-transition tail to the post-transition state, $\Delta C_{p,g} = 1.82 \pm 0.03$ W g⁻¹ K⁻¹ and $\Delta C_{p,c} = 2.46 \pm 0.04$ W g⁻¹ K⁻¹. For the overlapping melting peaks, $\Delta C_{p,m}$ does not converge (NA) due to purely mathematical artifact. However, if the peaks are sufficiently apart with sufficient baseline tail on each side, the cumulative $\Delta C_{p,m}$ can be reliably determined via the function (Table 9).

Conclusions

The analytical function $DSC_N(T)$ was developed to be fitted to the DSC experimental traces. It contains the equilibrium melting point (T_m^0), a parameter for the Arrhenius activation energy ($\alpha = E_a/(T_m^0)^2$), and a parameter for the Gaussian broadening (β). It is based on the assumption that the sample crystalline structure develops via a rate-limited growth governed by a simple Arrhenius activated process. The function also includes the Gaussian broadening to account for instrumental accuracy, non-isothermal conditions as governed by the rate of heating, sample mass, thermal conductivity, and may additionally reflect the possible presence and inhomogeneous incorporation of impurities. It was found that the function is remarkably versatile in providing an excellent fit to the DSC experimental data. It enables a very accurate analysis of the DSC data yielding reliable transition temperatures such as melting, crystallization, and liquid crystal transitions. A distinct advantage of $DSC_N(T)$ to the conventional analysis methods is that it allows the analysis of mixtures showing multiple overlapping peaks which can differentiate the phases more accurately. In addition, changes in enthalpy are obtained which are in excellent agreement with the reference standards in the literature. Using the same function, the glass transition can also be analyzed. Here, we used the same procedure as for the melting point where the primary feature is the step function and associated stepwise change of heat capacity ($\Delta C_{p,t}$). The value of $\Delta C_{p,m}$, although not very accurate, is a novel feature in $DSC_N(T)$ analytical model which is not usually available

in the standard analysis methods relying on the linear baseline selected by a data analyst.

Supplementary Information The online version contains supplementary material available at <https://doi.org/10.1007/s10973-023-12356-1>.

Acknowledgements The authors are grateful to Dr. Behrouz Eslami and Dr. Lars J. Bannenberg for their help in improving the Python scripts.

Open Access This article is licensed under a Creative Commons Attribution 4.0 International License, which permits use, sharing, adaptation, distribution and reproduction in any medium or format, as long as you give appropriate credit to the original author(s) and the source, provide a link to the Creative Commons licence, and indicate if changes were made. The images or other third party material in this article are included in the article's Creative Commons licence, unless indicated otherwise in a credit line to the material. If material is not included in the article's Creative Commons licence and your intended use is not permitted by statutory regulation or exceeds the permitted use, you will need to obtain permission directly from the copyright holder. To view a copy of this licence, visit <http://creativecommons.org/licenses/by/4.0/>.

References

- Demetzos C. Differential scanning calorimetry (DSC): a tool to study the thermal behavior of lipid bilayers and liposomal stability. *J Liposome Res.* 2008;18(3):159–73.
- Tanaka S. Theory of power-compensated DSC. *Thermochim Acta.* 1992;210:67–76.
- Raimo M. Kinetics of phase transformation of indium in the presence of polytetrafluoroethylene: implications for DSC measurements on polymers and their composites. *Int J Polym Sci.* 2015;1:2015.
- Crighton JS, Wilburn FW. The role of heat transfer in the production of DSC curves. *Thermochim Acta.* 1992;13(203):1–5.
- Bouzidi L, Boodhoo M, Humphrey KL, Narine SS. Use of first and second derivatives to accurately determine key parameters of DSC thermographs in lipid crystallization studies. *Thermochim Acta.* 2005;439(1–2):94–102.
- Ghanbari E, Krishnamurthy A, Picken SJ, Klop EA, Bannenberg LJ, van Esch J. Molecular arrangement and thermal properties of bisamide organogelators in the solid state. *Langmuir.* 2022;38(50):15782–95.
- Ahmed AK, Atiqullah M, Pradhan DR, Al-Harthi MA. Crystallization and melting behavior of i-PP: a perspective from Flory's thermodynamic equilibrium theory and DSC experiment. *RSC Adv.* 2017;7(67):42491–504.
- Coto B, Martos C, Espada JJ, Robustillo MD, Peña JL. Analysis of paraffin precipitation from petroleum mixtures by means of DSC: iterative procedure considering solid–liquid equilibrium equations. *Fuel.* 2010;89(5):1087–94.
- Martin JL, Martín JL. Kinetic analysis of an asymmetrical DSC peak in the curing of an unsaturated polyester resin catalysed with MEKP and cobalt octoate. *Polym Guildf.* 1999;40(12):3451–62.
- Wang G, Harrison IR. Polymer melting: heating rate effects on DSC melting peaks. *Thermochim Acta.* 1994;231:203–13.
- Davis GJ, Porter RS. Application of the differential scanning calorimeter to purity measurements. *J Therm Anal Calorim.* 1969;1(4):449–58.
- Kousksou T, Jamil A, Zeraoui Y. Enthalpy and apparent specific heat capacity of the binary solution during the melting process: DSC modeling. *Thermochim Acta.* 2012;541:31–41.

13. Müller A, Borchard W. Correlation between DSC curves and isobaric state diagrams. 3. Simulation of smeared DSC curves. *J Phys Chem B*. 1997;101(21):4307–12.
14. Feng L, Kamal MR. Distributions of crystal size from DSC melting traces for polyethylenes. *Can J Chem Eng*. 2004;82(6):1239–51.
15. Dong HB, Hunt JD. A numerical model for a heat flux DSC: Determining heat transfer coefficients within a DSC. *Mater Sci Eng A*. 2005;413:470–3.
16. Torfs JC, Deij L, Dorrepaal AJ, Heijens JC. Determination of arrhenius kinetic constants by differential scanning calorimetry. *Anal Chem*. 1984;56(14):2863–7.
17. Della Gatta G, Józwiak M, Brunetti B, Abate L. Enthalpies and entropies of fusion and of sublimation at the temperature 298.15 K of thiourea and sevenN-alkylthioureas. *J Chem Thermodyn*. 2000;32(8):979–97.
18. Brown ME. Determination of purity by differential scanning calorimetry (DSC). *J Chem Educ*. 1979;56(5):310.
19. Widmann G, Scherrer O. A new program for DSC purity analysis. *J Therm Anal*. 1991;37(8):1957–64.
20. Sharma BL, Jamwal R, Kant R. Thermodynamic and lamella models relationship for the eutectic system benzoic acid—cinnamic acid. *Cryst Res Technol*. 2004;39(5):454–64.
21. Popa VT, Segal E. Shape analysis of DSC ice melting endotherms. towards an estimation of the instrumental profile. *J Therm Anal Calorim*. 2002;69(1):149–61.
22. Archer DG. Enthalpy of fusion of bismuth: a certified reference material for differential scanning calorimetry. *J Chem Eng Data*. 2004;49(5):1364–7.
23. Van Miltenburg JC, Cuevas-Diarte MA. The influence of sample mass, heating rate and heat transfer coefficient on the form of DSC curves. *Thermochimica acta*. 1989;156(2):291–7.
24. Vyazovkin S. Activation energies and temperature dependencies of the rates of crystallization and melting of polymers. *Polymers*. 2020;12(5):1070.
25. Guillory JK. Book review of CRC handbook of chemistry and physics. 90th edition. *J Med Chem*. 2009;52(17):5560–5560.
26. L. Xu and R. Yang, Stearic acid/inorganic porous matrix phase change. 3(1), 1–11, 2019.
27. Ghosh S, Roy A. Crystal polymorphism of 8OCB liquid crystal consisting of strongly polar rod-like molecules. *RSC Adv*. 2021;11(9):4958–65.
28. Özgan Ş, Okumuş M. Thermal and spectrophotometric analysis of liquid crystal 8CB/8OCB mixtures. *Braz J Phys*. 2011;41(2–3):118–22.
29. Cordoyiannis G, Tripathi CSP, Glorieux C, Thoen J. Order of phase transitions and tricriticality in mixtures of octyloxycyanobiphenyl and nonyloxycyanobiphenyl liquid crystals: a high-resolution study by adiabatic scanning calorimetry. *Phys Rev E Stat Nonlinear Soft Matter Phys*. 2010;82(3):1–12.
30. Shang L, Fei Q, Zhang YH, Wang XZ, Di Fan D, Chang HN. Thermal properties and biodegradability studies of poly (3-hydroxybutyrate-co-3-hydroxyvalerate). *J Polym Environ*. 2012;20(1):23–8.
31. Laycock B, et al. Thermal properties and crystallization behavior of fractionated blocky and random polyhydroxyalkanoate copolymers from mixed microbial cultures. *J Appl Polym Sci*. 2014;131(19):1–19.

Publisher's Note Springer Nature remains neutral with regard to jurisdictional claims in published maps and institutional affiliations.